TUDelft

Delft University of Technology

Fluid–structure interaction analysis of a healthy aortic valve and its surrounding haemodynamics

Yin, Zhongjie; Armour, Chlöe; Kandail, Harkamaljot; O'Regan, Declan P.; Bahrami, Toufan; Mirsadraee, Saeed; Pirola, Selene; Xu, Xiao Yun

WILEY

Fluid–structure interaction analysis of a healthy aortic valve and its surrounding haemodynamics

Zhongjie Yin[1] | Chlöe Armour[1,2] | Harkamaljot Kandail[3] |
Declan P. O'Regan[4] | Toufan Bahrami[2,5] | Saeed Mirsadraee[2,6] |
Selene Pirola[1,7] 🔟 | Xiao Yun Xu[1] 🔟

[1]Department of Chemical Engineering, Imperial College London, London, UK

[2]National Heart and Lung Institute, Imperial College London, London, UK

[3]Medtronic Neurovascular, Irvine, California, USA

[4]Laboratory of Medical Sciences, Imperial College London, London, UK

[5]Department of Cardiothoracic Surgery, Royal Brompton and Harefield Hospitals NHS Trust, London, UK

[6]Department of Radiology, Royal Brompton and Harefield Hospitals NHS Trust, London, UK

[7]Department of BioMechanical Engineering, TU Delft, Delft, The Netherlands

Correspondence
Selene Pirola, Department of Bio-Mechanical Engineering, TU Delft, Delft, The Netherlands.
Email: s.pirola@tudelft.nl

Xiao Yun Xu, Department of Chemical Engineering, Imperial College London, South Kensington Campus, London, UK.
Email: yun.xu@imperial.ac.uk

Abstract

The opening and closing dynamics of the aortic valve (AV) has a strong influence on haemodynamics in the aortic root, and both play a pivotal role in maintaining normal physiological functions of the valve. The aim of this study was to establish a subject-specific fluid–structure interaction (FSI) workflow capable of simulating the motion of a tricuspid healthy valve and the surrounding haemodynamics under physiologically realistic conditions. A subject-specific aortic root was reconstructed from magnetic resonance (MR) images acquired from a healthy volunteer, whilst the valve leaflets were built using a parametric model fitted to the subject-specific aortic root geometry. The material behaviour of the leaflets was described using the isotropic hyperelastic Ogden model, and subject-specific boundary conditions were derived from 4D-flow MR imaging (4D-MRI). Strongly coupled FSI simulations were performed using a finite volume-based boundary conforming method implemented in FlowVision. Our FSI model was able to simulate the opening and closing of the AV throughout the entire cardiac cycle. Comparisons of simulation results with 4D-MRI showed a good agreement in key haemodynamic parameters, with stroke volume differing by 7.5% and the maximum jet velocity differing by less than 1%. Detailed analysis of wall shear stress (WSS) on the leaflets revealed much higher WSS on the ventricular side than the aortic side and different spatial patterns amongst the three leaflets.

1 | INTRODUCTION

The aortic valve (AV) is an essential part of the heart, maintaining unidirectional blood flow from the left ventricle to the aorta. However, current understanding of the interactions between haemodynamics in the aortic root and the opening and closing dynamics of the natural AV is incomplete. Standard in vivo imaging techniques, such as 2D echocardiography, can provide flow waveform in the left ventricular outflow tract (LVOT) and some haemodynamic functional parameters of the AV, such as mean pressure gradient and geometric orifice area (GOA).[1–3] Advanced imaging techniques, including electrocardiogram (ECG)-gated computed tomography (CT) and 4D-flow magnetic resonance imaging (MRI), have also been used to capture the AV dynamics and surrounding flow patterns,[4–8] but estimations of pressure and shear stress distributions are often based on simplified assumptions and are limited by the temporal and spatial resolution of the imaging techniques.[4]

An effective way to evaluate the dynamics of the AV and its influence on blood flow is through fluid–structure interaction (FSI) simulations whereby the region of interest can be modelled to obtain numerical predictions of the complex flow dynamics and associated biomechanical environment.[9] FSI analysis has already played an essential role in exploring the mechanisms of different AV diseases of varying severity,[9–18] evaluating the performance amongst different artificial AV products, and surgical implantation planning.[19–27] However, there are still some gaps in the current AV FSI studies. One of these is the lack of studies of natural, healthy valves in real, subject-specific conditions.

Several studies used idealised models to represent the valve and aorta geometry when simulating the healthy valve dynamics.[9,17,18,28,29] These studies showed valve motion, flow characteristics, wall shear stress (WSS) distribution of healthy AVs, and general differences from diseased or abnormal AVs. For example, compared to calcified[9,17] and bicuspid AVs,[17,18] healthy AVs tend to have a more symmetric and circular orifice area,[18,28] lower maximum velocity (1–2.25 m/s) at peak systole,[9,17,18,28] and smaller WSS magnitude (14.31 and 1.85 Pa systolic-averaged WSS on the ventricular and aortic side, respectively) on the leaflets.[17] However, idealised models of the aortic root and valve fail to reproduce the asymmetry amongst the three valve leaflets. Only a few studies adopted subject-specific geometries, but these only focused on finite element (FE) analysis of valve dynamics.[30–33] An additional limitation of existing studies is the lack of validation against in vivo data.

Therefore, in this study, we aimed to develop a strongly coupled FSI model of a healthy AV utilising as much subject-specific information as possible. Flow features predicted by the FSI model, including velocity streamlines, stroke volume (SV), maximum jet velocity and peak systolic spatial mean velocity, are compared against those observed in vivo, as extracted from the 4D-flow MRI data.

2 | MATERIALS AND METHODS

2.1 | Data acquisition and MR image processing

MR images of the aorta of a healthy 31-year-old female volunteer (height = 162 cm, weight = 65 kg) were acquired using a Siemens 3 T scanner at Hammersmith Hospital (London, UK). The study was approved by the National Research Ethics Service (17/EE/006) and the participant provided written informed consent. Cardio-respiratory gating was used in the MRI scan. Images were acquired in the sagittal plane, at 25 time points within the cardiac cycle, and with a voxel size of $2.00 \times 1.98 \times 1.98$ mm^3. Velocity encoding parameters for the three velocity components (anterior–posterior, foot–head and right–left) were 1.0, 1.4 and 1.3 m/s, respectively.

The aortic root was reconstructed from bright-blood MR images using Materialise Mimics (v24.0, Materialise, Leuven, Belgium). The aortic root model included the distal end of the LVOT and the ascending aorta. The raw 4D-flow MR images were processed using an in-house Python code,[34] which generated 3D velocities in the aorta at each time point, and flow waveform in the LVOT. The resulting aortic root geometry and LVOT flow waveform are shown in Figure 1.
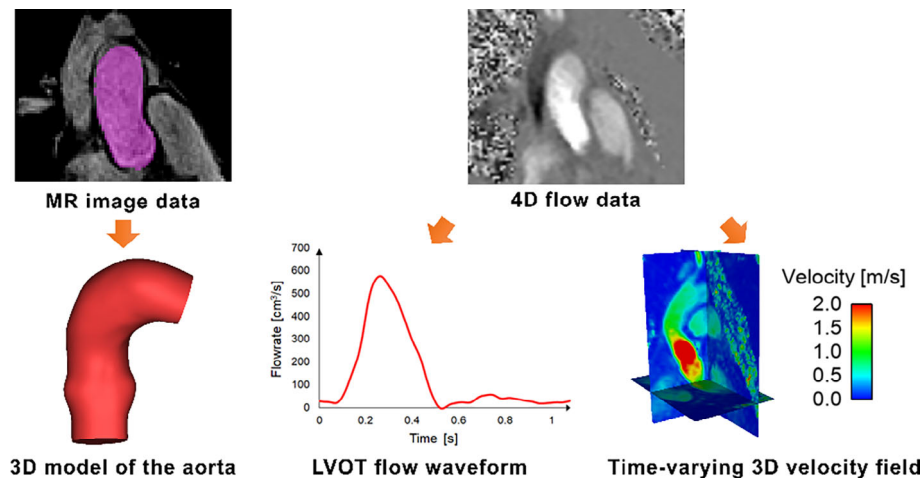
FIGURE 1 Reconstruction of the aortic root and LVOT flow waveform from MR images. LVOT, left ventricular outflow tract; MR, magnetic resonance.
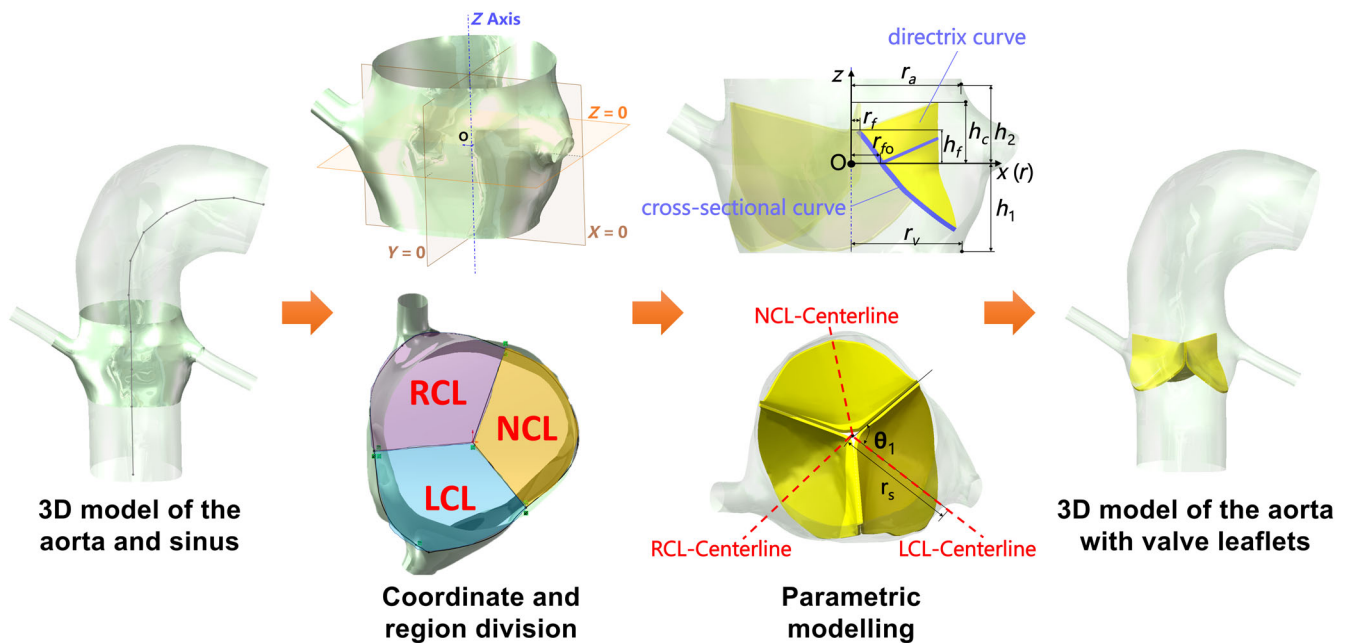
FIGURE 2 Workflow for creating aortic valve geometry and fitting it into a subject-specific aortic root model. LCL, left coronary leaflet; NCL, non-coronary leaflet; RCL, right coronary leaflet.

2.2 | Modelling the valve

It would be ideal to reconstruct the AV geometry from subject-specific images. However, the MR images for this case did not have sufficient resolution to provide geometric information about the valve leaflets. Therefore, a parametric model was required to describe the AV geometry. Due to its wide application in AV modelling,[28,35–38] the parametric model proposed by Haj-Ali et al.[39] was adopted, and adjusted to fit into the subject-specific aortic root geometry. The detailed steps are shown in Figure 2 and described below.

First, the 3D geometry of the sinus was isolated from the reconstructed aortic root geometry with its upstream and downstream cross-sectional planes being parallel. These planes corresponded to locations where the cross-sectional diameter began to expand (upstream plane) and stopped contracting (downstream plane). Then, a 3D Cartesian coordinate system was created, and the $z = 0$ plane was placed between the two parallel planes with the ratio of its distance to the upstream and downstream planes being 3:4.[39] The origin was defined as the intersection of the $z = 0$ plane and

the centreline. Finally, the left coronary leaflet (LCL), right coronary leaflet (RCL), and non-coronary leaflet (NCL) were created by first defining their centrelines. Here lines connecting the centre of the sinus to the left and right coronary orifices were defined as the centreline of LCL and RCL, and the angle bisector of these two lines was defined as the NCL centreline. Each leaflet surface was then created by sweeping the cross-sectional curve (Equation 1) along the directrix curve (Equation 2).

$$x = 2^{n-1} \frac{(r_a + r_s) \cos \theta_1 - 2r_{f_o}}{(r_a + r_s)^n \sin^n \theta_1} y^n + r_{f_o}, \tag{1}$$

$$z = \begin{cases} \dfrac{h_f}{r_f - r_{f_o}} \left(x - r_{f_o} \right) & (z \geq 0) \\ -h_1 + h_1 \left(\dfrac{r_v - x}{r_v - r_{f_o}} \right)^m & (z < 0) \end{cases}. \tag{2}$$

Values of the parameters in Equation (1) and Equation (2) for the three leaflets are listed in Table 1. Amongst these parameters, r_v, r_a, r_s, θ_1 and h_1, were measured from the subject-specific aorta geometry, and from which subsequent parameters were derived. Each swept surface was then smoothed and extruded with a thickness of .5 mm and cut by the aortic wall. The geometric models were built in SolidWorks (v2020, Dassault System, France) and smoothed and extruded in Meshmixer (Autodesk, USA).

2.3 | Geometric discretization

The aorta was defined as the fluid domain and was discretized through FlowVision (CAPVIDIA, Leuven, Belgium) with the sub-grid geometry resolution (SGGR) method.[40,41] The finite volume-based SGGR method implemented in FlowVision does not require global remeshing at every time step, whilst also having the advantage of being a boundary-conforming method which allows WSS to be adequately resolved. Local mesh adaptation was adopted to better resolve flow features in the proximity of the moving leaflets and in the sinus area. This was achieved through two steps: first, the whole fluid domain was meshed by an initial Cartesian grid with a characteristic dimension l_0; then, further refinement was performed with a four-layer adaptation following the moving leaflets.

The solid domain consisted of three leaflets and was discretized with C3D8R hexahedral elements in Abaqus (SIMULIA, Dassault System, France). C3D8R elements were adopted for their good geometric approximation,

TABLE 1 Values of parameters (defined in Figure 2) in Equation (1) and Equation (2) for the three leaflets. Some data were extracted from Haj-Ali et al.[39]

Parameter	Description	NCL	LCL	RCL
r_v	Sinus radius (ventricular end)	13.52 mm	12.63 mm	12.99 mm
r_a	Sinus radius (aortic end)	13.55 mm	12.02 mm	12.97 mm
r_s	Sinus radius ($z = 0$ plane)	14 mm	15.35 mm	15.58 mm
θ_1	Angle between the centreline of leaflet and neighbouring leaflet	60°	62.5°	57.5°
h_1	Distance between the ventricular end and $z = 0$ plane	7 mm		
h_2	Distance between the aortic end and $z = 0$ plane	$4 h_1/3$[39]		
h_f	Distance between the free edge of leaflets and $z = 0$ plane	$7 h_1/12$[39]		
h_c	Distance between the commissure of leaflets and $z = 0$ plane	$5 h_1/6$[39]		
r_{f_o}	Leaflet radius ($z = 0$ plane)	$.27 r_v$[39]		
r_f	Leaflet radius (free edge)	0		
n	Curve coefficient	1.5[39]		
m	Curve coefficient	1.25[39]		

Abbreviations: LCL, left coronary leaflet; NCL, non-coronary leaflet; RCL, right coronary leaflet.

numerical stability and contact handling capability, without making an excessive computational demand.[42,43] They can also reduce shear locking and capture the bending behaviour of the leaflets. The reasons for choosing solid instead of shell elements are twofold: first, using shell elements can result in self-intersection and negative volumes which would cause the simulation to fail; second, defining the two sides of the leaflets as boundary surfaces is crucial for accurately transferring information between the structural and fluid solvers. Solid elements provide a more robust framework for these boundary definitions, ensuring a stable and accurate FSI.

Mesh sensitivity tests were conducted for the fluid and solid domain separately to achieve the best compromise between accuracy and simulation time. The fluid mesh sensitivity test was performed on the whole aorta with a static, fully opened valve, and the same boundary conditions as in the FSI simulation. Average velocities at three planes distal to the valve and shear stresses on the leaflets were calculated and compared between consecutive meshes. The results (Table 2) showed that a global mesh size of $l_0 = .6$ mm (M4) with a four-layer local refinement near the leaflets (local mesh size $= 1/4 \times$ global mesh size) was adequate for good convergence in downstream velocity (<2% difference) and shear stress on the valve leaflets (<2% difference).

The solid mesh sensitivity test was performed on the valve pressurisation process by applying 10 mmHg on the ventricular side. A global solid mesh size of .25 mm and four elements in the thickness direction were found to be sufficient to achieve <5% difference in the GOA and maximum principal stress (MPS) compared to the finest mesh. These results were used to set up the computational FSI models, and the final fluid mesh and solid mesh numbers were $65 \times 236 \times 135$ and ~79,000, respectively.

2.4 | Tissue mechanical properties

The material of the leaflets was described using an isotropic, hyperelastic, third-order Ogden model.[44] Its strain energy function W can be written as:

$$W = \sum_{i=1}^{N} \frac{2\mu_i}{\alpha_i^2} \left(\overline{\lambda_1}^{\alpha_i} + \overline{\lambda_2}^{\alpha_i} + \overline{\lambda_3}^{\alpha_i} - 3 \right) \tag{3}$$

where μ_i and α_i are material constants and $\overline{\lambda_i}$ are the modified principal stretches. The parameters chosen for the leaflets were: $N = 3$, $\mu_1 = -47.75$ kPa, $\alpha_1 = 2$, $\mu_2 = 33.23$ kPa, $\alpha_2 = 4$, $\mu_3 = 14.60$ kPa, and $\alpha_3 = -2$. These material parameters (corresponding to the NCLs) were taken from the literature[12] wherein the material parameters were fitted to mechanical testing data acquired from tricuspid AV tissues and showed good agreement with the experimental curve.[45] Also, in their supplement materials, Emendi et al.[12] provided an FE test to show that the deformation was similar to the one

TABLE 2 Fluid mesh sensitivity test results.

Name	Grid number	Averaged velocity DOWN1 (m/s)	Averaged velocity DOWN2 (m/s)	Averaged velocity DOWN3 (m/s)	Averaged WSS NCL (Pa)	Averaged WSS RCL (Pa)	Averaged WSS LCL (Pa)
M1	265205	.594	.501	.528	5.196	6.135	5.527
M2	445380	.613	.520	.539	5.629	6.564	6.036
M3	613145	.613	.533	.556	5.949	6.454	6.246
M4	876705	.615	.515	.536	6.117	6.621	6.586
M5	1086959	.614	.522	.536	6.210	6.609	6.621
Difference (%)	M1-M2	3.2%	3.6%	2.1%	7.7%	6.5%	8.4%
	M2-M3	.1%	2.5%	3.1%	5.4%	1.7%	3.4%
	M3-M4	.3%	3.6%	3.8%	2.7%	2.5%	5.2%
	M4-M5	.04%	1.4%	.1%	1.5%	.2%	.5%

Note: DOWN1, DOWN2 and DOWN3 represent three downstream planes distal to the valve; NCL, RC stand for non-coronary, right coronary and left coronary leaflet, respectively.

obtained with an anisotropic Fung model fitted to the same experimental curve. A Rayleigh damping coefficient of $\alpha = 200\,\text{s}^{-1}$ was adopted for the leaflet material to consider the viscous damping effect. This value was chosen following test runs with the Rayleigh damping coefficient varying in the range of 0–$500\,\text{s}^{-1}$, and the results indicated that $\alpha = 200\,\text{s}^{-1}$ was enough to stabilise the valve motion without causing unrealistic energy dissipation due to excessive damping. The leaflets were assumed to be incompressible with a density of $1100\,\text{kg/m}^3$, and the aortic wall was assumed to be rigid.

2.5 | Loading and boundary conditions

In the structural domain, the attachment edges of all leaflets were constrained with all degrees of freedom (three degrees of movement). When the valve is closing and opening, its leaflets partly overlap with each other; this is known as coaptation in valve dynamics. Therefore, the definition of a contact model between the leaflets is required. No penetration between two parts is allowed, so the contact model between the three leaflets was defined using a 'hard' normal pressure-overclosure formulation.[46] The friction coefficient along the tangential direction is important for correctly mimicking valve dynamics. Previous research showed that larger friction coefficients could result in longer valve opening, closing and ejection times, as well as smaller valve orifice areas.[47] In the current study, tangential behaviours were defined as a penalty with a friction coefficient of .1 as adopted in other studies.[48,49] In the fluid domain, blood was assumed as an incompressible, Newtonian fluid with a density of $1060\,\text{kg/m}^3$ and a viscosity of .0035 Pa s. A time-dependent total pressure waveform was applied at the inlet (Figure 3). This pressure waveform was obtained by scaling a generic pressure waveform iteratively to match the subject-specific heart rate and the LVOT flow waveform extracted from 4D-flow MRI.

The descending aorta outlet was extended by a length of approximately five times the local diameter and a three-element Windkessel (3EWK) model[50] was applied at the outlet. Windkessel parameters were estimated based on mean pressure $\overline{P}$ and mean outlet flow $\overline{Q}$.[51] With these two parameters, the total resistance R_{total} and the compliance C were calculated by:

$$R_{\text{total}} = P_{\text{mean}}/Q_{\text{aortaoutlet}} \tag{4}$$

$$C = \tau/R_{\text{total}} \tag{5}$$
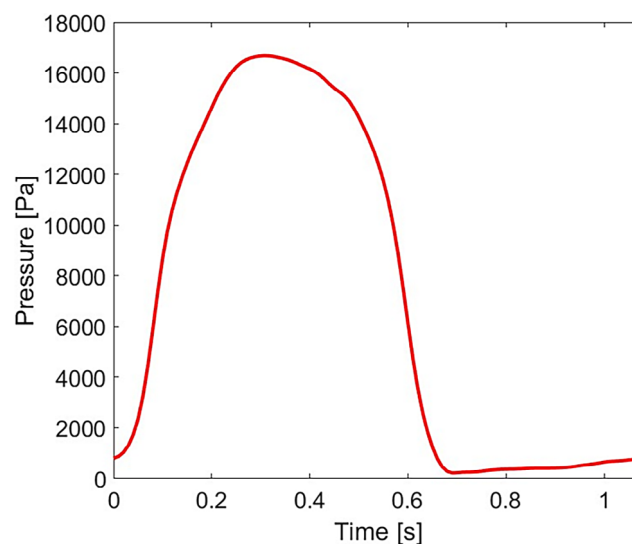
FIGURE 3 Total pressure waveform applied at the inlet in the aortic root.

TABLE 3   3EWK parameters for the model outlet.

R_p (kg/m^{4}s)	R_d (kg/m^{4}s)	C (m^{4}s^2/kg)
1.903×10^7	7.030×10^7	2.004×10^{-8}

Note: R_p: proximal resistance, R_d: distal resistance, C: compliance.

where $\tau = 1.79\,s$ was the time-constant of the exponential pressure-fall during diastole.[52] Finally, by assuming a circular outlet cross-section, the proximal resistance R_p could be calculated by the following equations:

$$R_p = \rho_f\, v_{\text{pulse}}/A \tag{6}$$

$$v_{\text{pulse}} = a_2/(2r/1000)^{b_2} \tag{7}$$

$$A = \pi r^2 \tag{8}$$

where ρ_f is fluid (blood) density, v_{pulse} is the pulse wave speed, A and r are the area and radius of the outlet cross-section measured from the 3D reconstructed model, $a_2 = 13.3$ and $b_2 = .3$ are fitted coefficients.[53] Since the total resistance R_{total} can also be described as the sum of proximal resistance R_p and distal resistance R_d, the distal resistance R_d was obtained by:

$$R_d = R_{\text{total}} - R_p \tag{9}$$

For the current simulation, a mean pressure $\overline{P} = 93.33\,\text{mmHg}$ (corresponding to LVBP of 120/80 mmHg) was used. This value also accounted for the pressure loss (13 Pa for this case) linked to the outlet extension, which was estimated by the Hagen–Poiseuille equation. The mean inlet flow was calculated from the 4D-flow MRI data. The resulting 3EWK parameters are given in Table 3.

2.6 | Numerical FSI set-up

The FSI model consisted of three parts: (i) the structural model defined in Abaqus Explicit 2019 (SIMULIA, Dassault System, France), (ii) the fluid model defined in FlowVision (CAPVIDIA, Leuven, Belgium) and (iii) the structural and fluid coupling, achieved through the external link function in FlowVision and co-simulation engine in Abaqus.

Every exchange step $\Delta t = t_{n+1} - t_n$ involved two sub-steps described below[21]:

1. In Abaqus, the pressure p_n was assumed to be constant throughout the step Δt and applied as a loading condition. The displacements of the nodes u_{n+1} were then solved based on the balance of momentum and transferred to FlowVision.
2. In FlowVision, the velocity at the fluid–structure interface was calculated by the displacements u_{n+1} from Abaqus. The Navier–Stokes equations were then solved to obtain the pressure p_{n+1} which was then passed on to Abaqus for the next time step.

The FSI exchange step $\Delta t = 10^{-4}\,$s should be the same as the time-step in the fluid solver because the latter was set as the master solver in FSI simulation with FlowVision. Three cardiac cycles were run for the FSI simulation on an Intel(R) Xeon(R) Silver 4114 CPU @ 2.20GHz 2.19 GHz (two processors), 128 GB RAM workstation and the results were derived from the third cycle.

2.7 | Analysis of results

Computational results for flow characteristics and valve motion were analysed at representative time points throughout the third cardiac cycle. All postprocessing was conducted in FlowVision Viewer, Abaqus Visualization module, Ensight,

Paraview and Matlab. Instantaneous flow patterns and blood velocities were compared with the corresponding 4D-flow MRI measurements for verification. The performance of the valve was evaluated by calculating the GOA, which is the anatomical area of an opening valve and can be calculated from a 2D projection of the AV leaflets' free edge on the aortic root cross-sectional area.[31] This parameter varies with the valve motion and is able to quantify the dynamic change in anatomical area of the AV orifice.[54]

WSS is an important haemodynamic parameter; its magnitude and directional variation have been correlated with aorto-pathology and valve degeneration.[55,56] Peak-systolic (PWSS) and time-averaged WSS over the cardiac cycle (TAWSS) were visualised on the aortic wall and leaflets and the spatial averaged values of these two variables in different regions were also quantitatively compared.

3 | RESULTS

3.1 | Flow patterns and comparison with 4D-flow MRI

Figure 4 shows velocity 3D volume rendering contours obtained from FSI, alongside the corresponding 4D-flow MRI measurements. At mid-systolic acceleration (t_1), the pressure gradient across the valve forms a strong forward jet
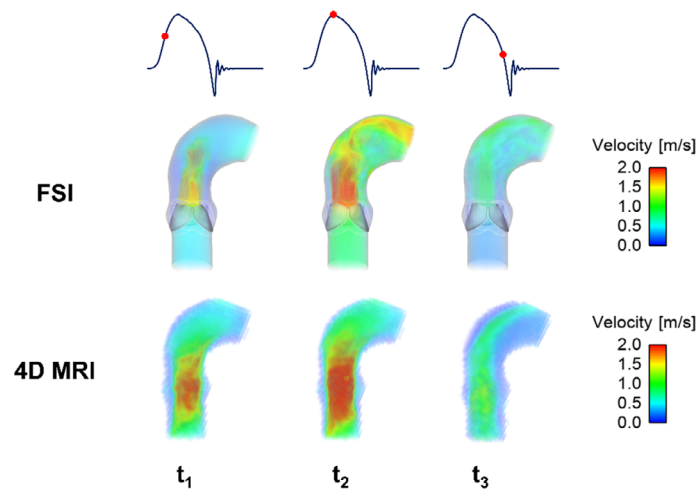
FIGURE 4 Velocity contours at three representative time points (t_1: acceleration phase, t_2: peak systole and t_3: deceleration phase) for the FSI and 4D-flow MRI data. FSI, fluid–structure interaction; MRI, magnetic resonance imaging.
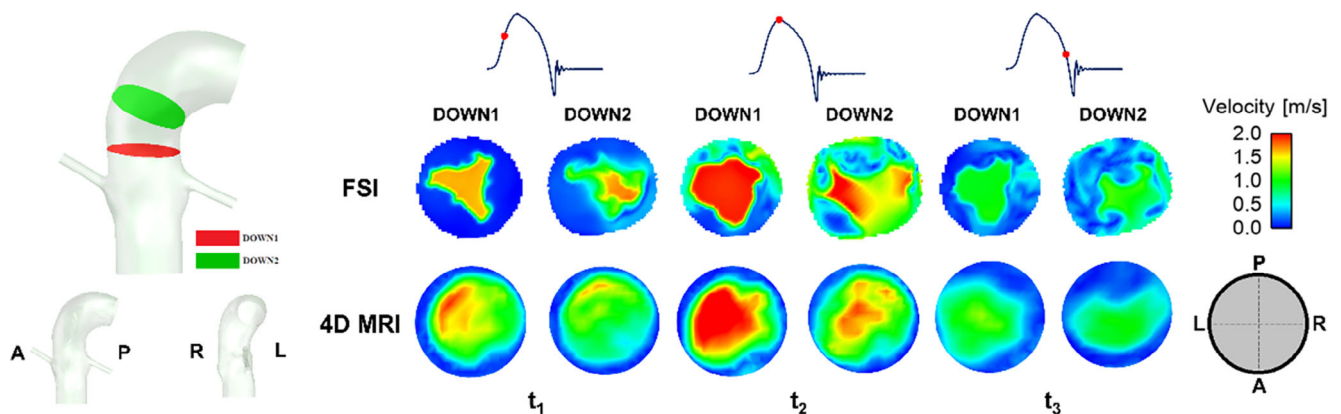
FIGURE 5 Velocity contours at two cross sections downstream of the valve at three representative time points (t_1: acceleration phase, t_2: peak systole, and t_3: deceleration phase) for the FSI and 4D-flow MRI data. A, P, R and L represent anterior, posterior, right and left direction, respectively.

flow, pushing the valve open, and the surrounding velocity is much lower than in the central area. During peak systole (t_2), the jet flow increases as a result of larger opening area, hitting the outer wall and changing its direction following the arch curvature. During late-systolic deceleration (t_3), the velocity magnitude is significantly decreased, and the valve begins to close. Finally, the valve is fully closed by mid-diastole as shown later.

Overall, the flow patterns show good qualitative agreement between the FSI simulation and 4D-flow MRI. In the area downstream of the valve, the general spatial distribution is similar except in the aortic arch where higher velocities were observed in the FSI model. This was likely caused by the exclusion of supra-aortic branches in the FSI model, as approximately 20%–30% of the aortic flow is expected to be diverted to the branches, thereby reducing flow within the arch. In the area upstream of the valve, the FSI simulation shows a uniform forward flow as a result of the flat velocity profile assumption at the model inlet. By contrast, the corresponding 4D-flow MRI shows a high velocity core that mirrors the spatial pattern after the valve.

Figure 5 shows comparisons of velocity contours at two cross sections distal from the valve. At the plane closer to the valve (DOWN1), results from the FSI simulation display a clear triangle-shaped flow pattern at t_1, but this pattern is

TABLE 4 Quantitative comparison of key parameters derived from FSI simulation results and 4D-flow MRI. The jet velocity and peak systole spatial mean velocity were measured at the plane 15 mm above the sinus plane.

	4D-flow MRI	FSI	Difference (%)
SV (mL)	134.32	124.24	−7.50%
Max jet velocity (m/s)	2.388	2.367	−.88%
Peak systolic spatial mean velocity (m/s)	1.041	1.043	.19%

Abbreviations: FSI, fluid–structure interaction; MRI, magnetic resonance imaging; SV, stroke volume.
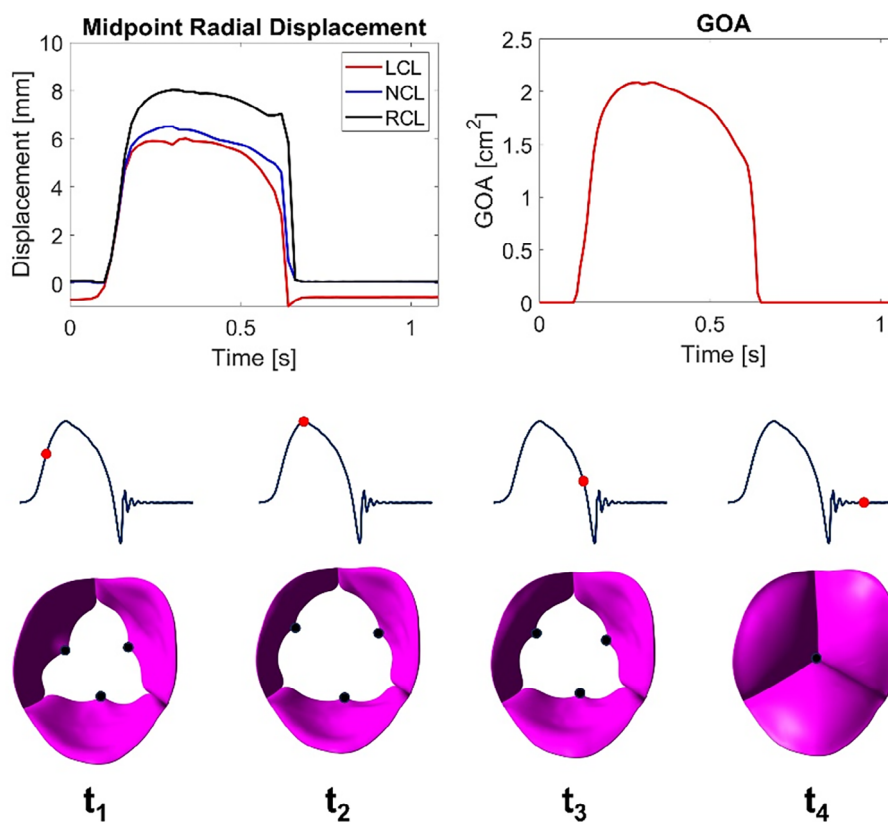
FIGURE 6 Variations of valve dynamic parameters (midpoint displacements for LCL, NCL, RCL and GOA) and orifice areas (looking from the LVOT, vertical to the centreline) throughout the cardiac cycle. GOA, geometric orifice area; LCL, left coronary leaflet; LVOT, left ventricular outflow tract; NCL, non-coronary leaflet; RCL, right coronary leaflet.

not observed in the corresponding 4D-flow MRI. As the valve becomes fully opened at t_2, the flow pattern becomes similar between the FSI and 4D-flow MRI. Further distal from the valve (DOWN2), both FSI and 4D-flow MRI results show a reduction in central jet velocity and more uniform velocity distribution. At both downstream planes, FSI results show a more symmetric distribution whereas the 4D flow velocities are skewed to the left. This is likely related to the flat velocity profile assumed at the model inlet and differences in the geometric shape and mechanical properties of the modelled leaflets compared to the real leaflets.

A quantitative comparison of key parameters was made between the simulation results and 4D-flow MRI data (Table 4). Here, stroke volume was calculated by integrating the flow rate over the time during systole. The jet velocity and peak systolic spatial mean velocity were measured at the DOWN 1 plane defined in Figure 5. Compared to the 4D-flow MRI, the FSI simulation predicted a slightly smaller SV, almost identical maximum jet velocity and peak systolic spatial mean velocity (Table 4).

3.2 | Valve dynamics

Figure 6 presents dynamic parameters of the valve throughout the cardiac cycle and shows the valve orifice areas at four distinct time points. The midpoint radial displacements for the three leaflets with respect to their initial unloaded positions all reach a maximum at peak systole. The RCL has the largest midpoint radial displacement (8.03 mm, compared to the LCL at 6.02 mm and the NCL at 6.51 mm). When the valve is closed, the RCL and NCL midpoint radial displacements are greater than zero, whereas the LCL midpoint radial displacement is less than zero, which means the valve is slightly tilted opposite the LCL radial direction. The time-varying GOA also reaches a maximum (2.09 cm^2) at peak systole, before reducing to zero when the valve is closed. The orifice shape is triangular during systolic acceleration (t_1) and deceleration (t_3), and slightly more circular at peak systole (t_2).

3.3 | WSS on the aorta and the leaflets

Figure 7 shows the PWSS and TAWSS on the aorta. Compared to the aortic root (Zone 2 and Zone 3), WSS is much higher in the distal ascending aorta (Zone 4) where the maximum PWSS and TAWSS reach 8.00 Pa and 2.67 Pa, respectively. The lowest WSS is in the sinus downstream of the valve (Zone 3) where PWSS and TAWSS are 3.29 Pa and 1.03 Pa, respectively. The spatial variations of PWSS and TAWSS along the aorta follow the same pattern. Note that quantitative analysis of WSS in Zones 1, 5 and 6 is not included because the main region of interest is the aortic root. In
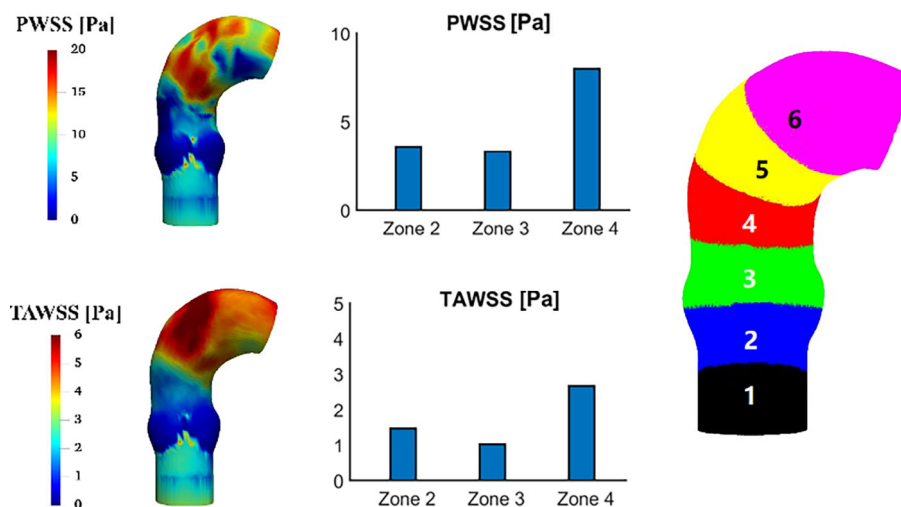
FIGURE 7 PWSS and TAWSS on the aorta (3D distribution and average values in different zones). Zone 1, Zone 5 and Zone 6 are excluded from the bar chart for they are not the region of interest. PWSS, peak-systolic wall shear stress; TAWSS, time-averaged wall shear stress.
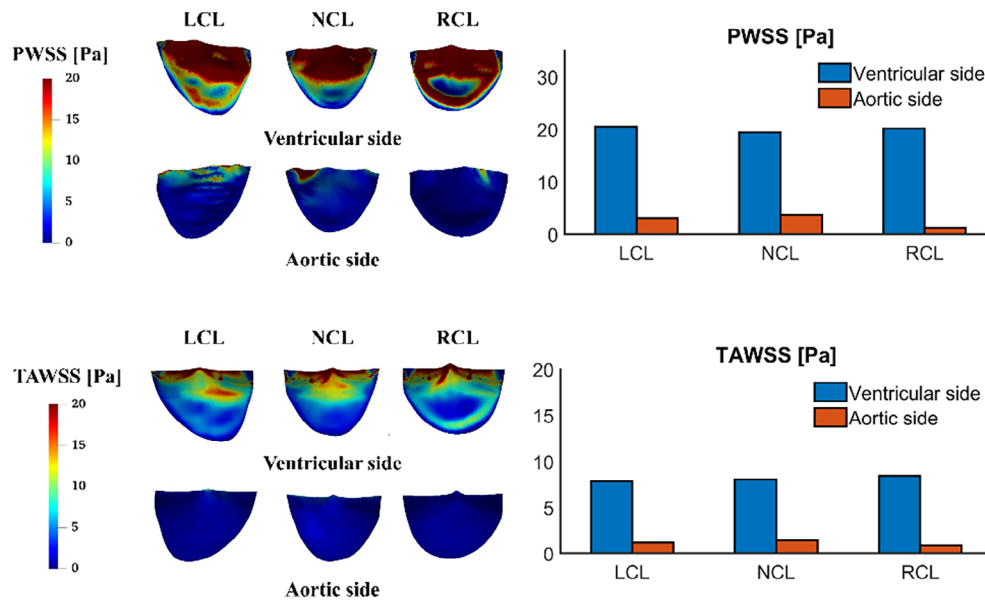
FIGURE 8 PWSS and TAWSS on the leaflets (3D distribution and average values on ventricular and aortic sides). LCL, left coronary leaflet; NCL, non-coronary leaflet; PWSS, peak-systolic wall shear stress; RCL, right coronary leaflet; TAWSS, time-averaged wall shear stress.
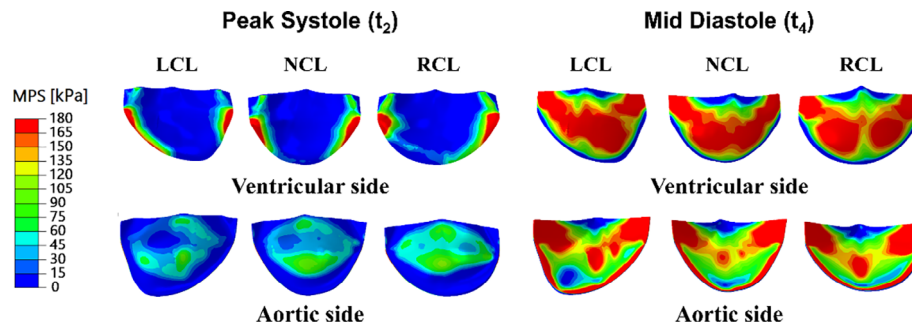
FIGURE 9 Maximum principal stress (MPS) distributions on the ventricular and aortic sides of the leaflets at peak systole and mid-diastole. LCL, left coronary leaflet; NCL, non-coronary leaflet; RCL, right coronary leaflet.

addition, values of WSS in these regions are affected by the inlet boundary condition (Zone 1) and the exclusion of supra-aortic branches (Zones 5 and 6).

Figure 8 shows the PWSS and TAWSS contours on the two sides of the leaflets. Both PWSS and TAWSS are higher on the ventricular side than the aortic side. On the ventricular side, PWSS magnitudes are very similar amongst the three leaflets (20.47, 20.07 and 19.36 Pa for LCL, RCL and NCL, respectively), and the same applies to TAWSS (7.84, 8.40 and 8.01 Pa for LCL, RCL and NCL, respectively). On the aortic side, the NCL has the largest PWSS (3.69 Pa compared to the 3.00 and 1.12 Pa for LCL and RCL, respectively) and the largest TAWSS (1.40 Pa compared to the 1.15 and .86 Pa for LCL and RCL, respectively). High WSS values are mostly located near the top edges of the leaflets on the ventricular side.

3.4 | Mechanical stress on the leaflets

Figure 9 shows the MPS distribution on the leaflets at peak systole and mid-diastole. The MPS magnitude is higher at mid-diastole when the valve is fully closed than at peak systole. At peak systole, the highest MPS region is located near the attachment edge on the ventricular side. At mid-diastole, the highest MPS occurs at the coaptation area of both sides and attachment edge of the aortic side.
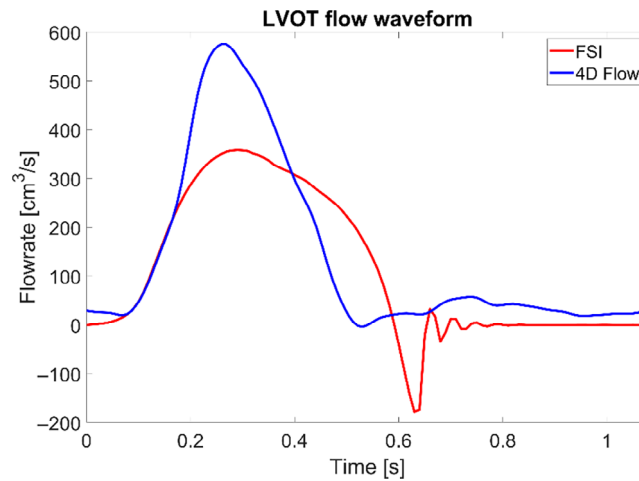
FIGURE 10   LVOT flow waveform extracted from 4D flow MRI and FSI simulation. FSI, fluid–structure interaction; LVOT, left ventricular outflow tract; MRI, magnetic resonance imaging.

4 | DISCUSSION

In this study, a workflow for FSI simulation of natural AV motion and the surrounding haemodynamics has been developed and applied to a healthy volunteer. It includes a subject-specific geometric model created by combining the aortic root reconstructed from MR images and the AV created by a parametric model. Two-way fully coupled FSI simulations were performed under subject-specific flow conditions. The FSI model is capable of simulating the entire cardiac cycle, allowing the AV to fully open and close. Simulation results are also compared with 4D-flow MRI in an initial attempt to validate the model.

4.1 | Model validation

As an advanced technology in cardiovascular imaging, 4D-flow MRI provides a time-resolved 3D velocity field which not only serves as a valuable input to determine subject-specific boundary conditions but can also be used to validate computational models. This method has already been applied to cardiovascular haemodynamics, both in studies related[12,57,58] and unrelated[59–61] to the AV.

The present study also adopted boundary conditions derived from 4D-flow MRI data. This was done by using the LVOT flow waveform derived from 4D-flow MRI to tune the inlet total pressure waveform and outlet 3EWK parameters. Instead of directly imposing the flow waveform at the inlet, a total pressure waveform was applied to allow a more physiological control over the dynamics of the AV; indeed, in vivo it is the pressure difference between the aortic and ventricular side that drives the valve dynamics. However, reproducing the MRI-derived flow waveform has proved challenging, even though a good match in SV, maximum jet velocity and peak systolic spatial mean velocity was achieved, as shown in Table 4. Figure 10 shows the LVOT flow waveforms extracted from the FSI simulation and MRI. Clearly, the peak flow rate reached by the FSI simulation was much lower than that derived from MRI, whilst the duration of systole was longer. In addition, it was observed in Figure 5 that the FSI jet flow areas on the downstream cross sections were smaller than those from MRI. All these indicate that the FSI simulation underestimated valve opening area and predicted a slower closing, causing the valve to open for longer. There are multiple reasons leading to these discrepancies. First, the mechanical properties of the valve were based on previously published data, which might be stiffer for the simulated valve. Second, the leaflet geometry and thickness were not subject-specific, which can affect the valve opening and closing dynamics (to be discussed later). Third, the effects of aortic wall compliance and coronary flow on valve motion were neglected.

In addition to the factors mentioned above, it must be noted that 4D flow MRI has its own limitations, especially its relatively low temporal and spatial resolution.[4] In the present study, 4D flow MRI was acquired at 25 time points over a cycle with a voxel size of $2.00 \times 1.98 \times 1.98$ mm^3. Flow rate was likely to be overestimated as it was calculated as the sum of pixel velocity multiplied by the pixel area in a chosen cross section. Also, low velocities have low signal-noise

ratio, which could further increase errors in regions of low velocity and during diastole. Finally, the time points for comparison between the FSI simulation and 4D flow MRI were not exactly the same, and these were selected after scaling to match the stage of valve opening.

4.2 | Common characteristics for a healthy AV

The simulation results presented in this study show the haemodynamic characteristics and biomechanical behaviour of a healthy valve. Specifically, the AV presented an approximately circular orifice shape at peak systole (Figure 6),[18,62] and a flow recirculation zone was observed between the leaflets and the sinus (Figure 4), which could help prevent blood stagnation.[9,13,29] The AV reached a maximum GOA of 2.09 cm^2 (Figure 6), compared to the maximum GOA of around 2 cm^2 reported by Chen and Luo.[63] The maximum jet velocity was 2.37 m/s (Table 4), which is comparable to the maximum jet velocity of 2.25 m/s reported by Salman et al.,[17] and 2.27 m/s reported by Cai et al.[62] Compared to previous idealised valve models, the most notable differences captured by the patient-specific model in this study are asymmetric features in AV kinematics and the surrounding haemodynamics.

The magnitude and spatial distribution of WSS are dictated by local flow patterns and geometrical features. During systole, the jet flow directly impacted on the distal and outer curvature of the aorta (Figure 4), resulting in higher PWSS and TAWSS compared to the proximal, inner wall of the aorta (Figure 7).[10] The high WSS on the ventricular side of the leaflets was generated by the forward jet flow with a high velocity magnitude through the AV.[10,17] In contrast, the low velocity flow recirculation zones in the aortic sinuses had low PWSS and TAWSS (Figure 8).[10,17] The orifice area formed by the three leaflets decreased moving from the LVOT into the aorta, thus PWSS and TAWSS were the highest on the top edges of the leaflets (Figure 8).[64–66]

Regarding mechanical stress on the leaflets, MPS values were larger during mid-diastole than at peak systole (Figure 9).[33,67] This was mainly due to the high absolute transvalvular pressure in diastole (Figure 11). During mid-diastole, the MPS was high in the commissure and coaptation area (Figure 9), with stress concentration at the sharp corner of the top edge, which led to higher magnitudes there.[32] This was due to the attachment edges of the leaflets being constrained in the FSI model. A similar pattern has been reported by others[28,31] when the valve leaflets were tied with an aortic wall that has a much stiffer material property than the leaflets.

Several factors influence the opening and closing dynamics of the valve and the surrounding haemodynamics. These include the valve's height–radius (H–R) ratio ($H = h_1 + h_2$, $R = r_v$ in Figure 2; Table 1),[69] leaflet thickness,[58] and its material properties,[70] coronary flow[71] and aortic wall compliance.[68] To understand how H–R ratio and leaflet material properties may affect valve opening and closing, decoupled FE simulations were performed on the same AV geometry (H–R ratio = 1.1) and two additional cases: one with a higher H–R ratio (=1.5) and another with different material properties described by the anisotropic Holzapfel–Gasser–Ogden model. The strain-energy function of the HGO model is expressed as[72,73]:
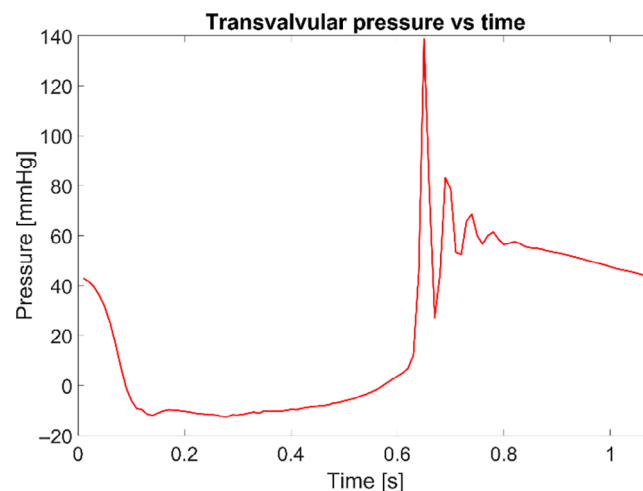
FIGURE 11 Transvalvular pressure throughout the cardiac cycle. The oscillation in this figure indicates the water hammer effect due to the sudden pressure drop when the valve is closed.[68]

TABLE 5 Maximum and minimum GOA with decoupled FE simulations of different H–R ratio and material properties.

Case description	Maximum GOA (cm^2)	Minimum GOA (cm^2)
Decoupled FE simulation (H–R ratio = 1.1)	2.43	0
Decoupled FE simulation (H–R ratio = 1.5)	2.16	.17
Decoupled FE simulation with anisotropic material properties from Ref. 74	2.53	.03

Abbreviations: GOA, geometric orifice area; FE, finite element.

$$W = C_{10}\left(\bar{I}_1 - 3\right) + \frac{k_1}{2k_2}\sum_{i=1}^{2}\left(e^{\left[k_2\left(\kappa\bar{I}_1 + (1-3\kappa)\bar{I}_{4i} - 1\right)\right]^2} - 1\right) \tag{10}$$

where C_{10}, k_1, k_2 are material parameters, $\bar{I}_1$ is the first invariant of the deviatoric deformation tensor, $\bar{I}_{4i}$ is the squared stretch along the fibre direction, and κ is the dispersion parameter which determines the level of dispersion in fibre orientation. In the current study, the parameters chosen for the leaflets were taken from the literature[74]: $C_{10} = 41$ kPa, $k_1 = 14710$ kPa, $k_2 = 3.83$, and $\kappa = .05$. One fibre-family was adopted with the HGO model and the fibre orientations were aligned along the circumferential direction of each leaflet.[75] These simulations were run by applying the same transvalvular pressure obtained from the FSI simulation (Figure 11). Table 5 compares the maximum and minimum GOA obtained from the decoupled FE simulations. The preliminary results indicated that the H–R ratio and material properties of the leaflets had notable effects on the valve dynamics, and inappropriate choice of these parameters could lead to incomplete closure of the AV during diastole. Specifically, increasing H–R ratio was found to lead to incomplete coaptation,[69] which has been confirmed by the non-zero minimum GOA when H–R ratio was increased from 1.1 to 1.5. It is also worth noting that the decoupled FE simulation predicted a higher maximum GOA (2.43 cm^2) compared to the FSI simulation, and a similar finding was reported by Mao et al.[76] Likewise, valve material properties also affect valve closing, and the stress–strain curves in Ref. 12 and 74 represent a stiffer material than the current model, causing incomplete closure of the valve under the same loading condition. In other studies, valve thickness,[58] coronary flow[71] and aortic wall compliance[68] were also found to have varying impact on AV dynamics and the surrounding haemodynamics.

4.3 | Limitations

The present study has several limitations. First, the 4D-flow MR and bright-blood MR images did not have sufficient resolution to provide information on the shape and location of the valve leaflets. High-resolution CT images could serve this purpose,[77] but CT scans are not usually performed on healthy volunteers. Thus, a parametric model was utilised and modified to match subject-specific dimensions of the aortic root to build three unique valve leaflets. Further, it was not possible to estimate the amount of coronary flow, which has been shown to affect WSS measurement.[71] Second, the FSI model ignored the effects of turbulence during the systolic ejection phase,[19,66,78] anisotropic behaviour of the valve leaflets,[74,77] aortic compliance[68,79] and pre-stresses in the valve leaflets.[31] These factors have been suggested to have minor impacts on the valve dynamics and haemodynamics.[68,76] For example, the compliant wall assumption could dampen the oscillations (Figure 11) when the valve is closing, but it did not affect the flow rate during the ejection phase.[68] Finally, only one healthy AV was included to demonstrate the utility of the simulation workflow. Future work will focus on improving the physiological fidelity of the model and extending its application to diseased AV and bio-prosthetic valves.

5 | CONCLUSIONS

The present study established a subject-specific FSI workflow capable of simulating the motion of a healthy AV throughout the cardiac cycle. The simulation results were in good agreement with the subject-specific 4D-flow MRI data and showed the common haemodynamic characteristics and biomechanical behaviour of a healthy valve. The FSI model also allowed detailed analysis of WSS on each leaflet, and our results revealed different spatial patterns and magnitudes amongst the three leaflets.

CONFLICT OF INTEREST STATEMENT

The authors declare no conflicts of interest.

DATA AVAILABILITY STATEMENT

The data that support the findings of this study are available on request from the corresponding author. The data are not publicly available due to privacy or ethical restrictions.

ORCID

Selene Pirola https://orcid.org/0000-0003-4368-3940
Xiao Yun Xu https://orcid.org/0000-0002-8267-621X

REFERENCES

1. Bach DS. Echo/Doppler evaluation of hemodynamics after aortic valve replacement: principles of interrogation and evaluation of high gradients. *JACC Cardiovasc Imaging*. 2010;3(3):296-304.
2. Everett RJ, Newby DE, Jabbour A, Fayad ZA, Dweck MR. The role of imaging in aortic valve disease. *Curr Cardiovasc Imaging Rep*. 2016;9:21.
3. Hahn RT, Nicoara A, Kapadia S, Svensson L, Martin R. Echocardiographic imaging for transcatheter aortic valve replacement. *J Am Soc Echocardiogr*. 2018;31(4):405-433.
4. Soulat G, McCarthy P, Markl M. 4D flow with MRI. *Annu Rev Biomed Eng*. 2020;22:103-126.
5. Hope MD, Meadows AK, Hope TA, et al. Images in cardiovascular medicine. Evaluation of bicuspid aortic valve and aortic coarctation with 4D flow magnetic resonance imaging. *Circulation*. 2008;117(21):2818-2819.
6. von Knobelsdorff-Brenkenhoff F, Trauzeddel RF, Barker AJ, Gruettner H, Markl M, Schulz-Menger J. Blood flow characteristics in the ascending aorta after aortic valve replacement—a pilot study using 4D-flow MRI. *Int J Cardiol*. 2014;170(3):426-433. Blood flow characteristics in the ascending aorta after aortic valve replacement—a pilot study using 4D-flow MRI.
7. Garcia J, Barker AJ, Markl M. The role of imaging of flow patterns by 4D flow MRI in aortic stenosis. *JACC Cardiovasc Imaging*. 2019;12(2):252-266.
8. Lenz A, Petersen J, Riedel C, et al. 4D flow cardiovascular magnetic resonance for monitoring of aortic valve repair in bicuspid aortic valve disease. *J Cardiovasc Magn Reson*. 2020;22(1):29.
9. Mutlu O, Salman HE, Yalcin HC, Olcay AB. Fluid flow characteristics of healthy and calcified aortic valves using three-dimensional Lagrangian coherent structures analysis. *Fluids*. 2021;6(6):203.
10. Cao K, Atkins SK, McNally A, Liu J, Sucosky P. Simulations of morphotype-dependent hemodynamics in non-dilated bicuspid aortic valve aortas. *J Biomech*. 2017;50:63-70.
11. Chandra S, Rajamannan NM, Sucosky P. Computational assessment of bicuspid aortic valve wall-shear stress: implications for calcific aortic valve disease. *Biomech Model Mechanobiol*. 2012;11(7):1085-1096.
12. Emendi M, Sturla F, Ghosh RP, et al. Patient-specific bicuspid aortic valve biomechanics: a magnetic resonance imaging integrated fluid-structure interaction approach. *Ann Biomed Eng*. 2021;49(2):627-641.
13. Ghasemi Pour MJ, Hassani K, Khayat M, Etemadi HS. Modeling of aortic valve stenosis using fluid-structure interaction method. *Perfusion*. 2021;37(4):267659121998549.
14. Lavon K, Morany A, Halevi R, et al. Progressive calcification in bicuspid valves: a coupled hemodynamics and multiscale structural computations. *Ann Biomed Eng*. 2021;49(12):3310-3322.
15. Luraghi G, Matas JFR, Beretta M, Chiozzi N, Iannetti L, Migliavacca F. The impact of calcification patterns in transcatheter aortic valve performance: a fluid-structure interaction analysis. *Comput Methods Biomech Biomed Engin*. 2020;1-9:375-383.
16. Qin T, Caballero A, Mao W, et al. Patient-Specific Analysis of Bicuspid Aortic Valve Hemodynamics Using a Fully Coupled Fluid-Structure Interaction (FSI) Model. *Comput Biol Med*. 2021;172:108191.
17. Salman HE, Saltik L, Yalcin HC. Computational analysis of wall shear stress patterns on calcified and bicuspid aortic valves: focus on radial and Coaptation patterns. *Fluids*. 2021;6(8):287.
18. Yan W, Li J, Wang W, Wei L, Wang S. A fluid-structure interaction study of different bicuspid aortic valve phenotypes throughout the cardiac cycle. *Front Physiol*. 2021;12:716015.

19. Becsek B, Pietrasanta L, Obrist D. Turbulent systolic flow downstream of a bioprosthetic aortic valve: velocity spectra, wall shear stresses, and turbulent dissipation rates. *Front Physiol.* 2020;11:577188.

20. Kandail HS, Trivedi SD, Shaikh AC, et al. Impact of annular and supra-annular CoreValve deployment locations on aortic and coronary artery hemodynamics. *J Mech Behav Biomed Mater.* 2018;86:131-142.

21. Sodhani D, Reese S, Aksenov A, et al. Fluid-structure interaction simulation of artificial textile reinforced aortic heart valve: validation with an in-vitro test. *J Biomech.* 2018;78:52-69.

22. Zhu G, Ismail MB, Nakao M, Yuan Q, Yeo JH. Numerical and in-vitro experimental assessment of the performance of a novel designed expanded-polytetrafluoroethylene stentless bi-leaflet valve for aortic valve replacement. *PLoS One.* 2019;14(1):e0210780.

23. Morganti S, Brambilla N, Petronio AS, Reali A, Bedogni F, Auricchio F. Prediction of patient-specific post-operative outcomes of TAVI procedure: the impact of the positioning strategy on valve performance. *J Biomech.* 2016;49(12):2513-2519.

24. Pasta S, Cannata S, Gentile G, et al. Simulation study of transcatheter heart valve implantation in patients with stenotic bicuspid aortic valve. *Med Biol Eng Comput.* 2020;58(4):815-829.

25. Tzamtzis S, Viquerat J, Yap J, Mullen MJ, Burriesci G. Numerical analysis of the radial force produced by the Medtronic-CoreValve and Edwards-SAPIEN after transcatheter aortic valve implantation (TAVI). *Med Eng Phys.* 2013;35(1):125-130.

26. Vahidkhah K, Barakat M, Abbasi M, et al. Valve thrombosis following transcatheter aortic valve replacement: significance of blood stasis on the leaflets. *Eur J Cardiothorac Surg.* 2017;51(5):927-935.

27. Li C, Tang D, Yao J, et al. Bioprosthetic valve size selection to optimize aortic valve replacement surgical outcome: a fluid-structure interaction modeling study. *Comput Model Eng Sci.* 2021;127(1):159-174.

28. Morany A, Lavon K, Gomez Bardon R, et al. Fluid-structure interaction modeling of compliant aortic valves using the lattice Boltzmann CFD and FEM methods. *Biomech Model Mechanobiol.* 2023;22:837-850.

29. Tango AM, Salmonsmith J, Ducci A, Burriesci G. Validation and extension of a fluid–structure interaction model of the healthy aortic valve. *Cardiovasc Eng Technol.* 2018;9(4):739-751.

30. Rossini G, Caimi A, Redaelli A, Votta E. Subject-specific multiscale modeling of aortic valve biomechanics. *Biomech Model Mechanobiol.* 2021;20(3):1031-1046.

31. Votta E, Presicce M, Della Corte A, et al. A novel approach to the quantification of aortic root in vivo structural mechanics. *Int J Numer Method Biomed Eng.* 2017;33(9):e2849.

32. Liang L, Kong F, Martin C, et al. Machine learning-based 3-D geometry reconstruction and modeling of aortic valve deformation using 3-D computed tomography images. *Int J Numer Method Biomed Eng.* 2017;33(5):e2827.

33. Morany A, Lavon K, Bluestein D, Hamdan A, Haj-Ali R. Structural responses of integrated parametric aortic valve in an electro-mechanical full heart model. *Ann Biomed Eng.* 2021;49(1):441-454.

34. Saitta S. saitta-s/flow4D: flow4D. In: Zenodo. 2022. doi:10.5281/zenodo.7236015

35. Geng Y, Wang Y, Ye Y, et al. An approach for designing patient-specific prosthetic aortic valves based on CT images using fluid-structure interaction (FSI) method. *2023 Comput Cardiol Conference (CinC).* 2023;50:1-4.

36. Pase G, Brinkhuis E, De Vries T, Kosinka J, Willems T, Bertoglio C. A parametric geometry model of the aortic valve for subject-specific blood flow simulations using a resistive approach. *Biomech Model Mechanobiol.* 2023;22(3):987-1002.

37. Raza M, Kingora K, Sadat H. *Molding Aortic Valve Hemodynamics Using a Novel Immersed Boundary Method.* TACCSTER 2022; 2022.

38. Wang Y, He F, Hao P, Zhang X. A fluid-structure interaction simulation on the impact of intervenient ventricular assist devices on aortic valves. *Comput Methods Programs Biomed.* 2024;254:108270.

39. Haj-Ali R, Marom G, Ben Zekry S, Rosenfeld M, Raanani E. A general three-dimensional parametric geometry of the native aortic valve and root for biomechanical modeling. *J Biomech.* 2012;45(14):2392-2397.

40. Aksenov A, Dyadkin A, Pokhilko V. Overcoming of barrier between CAD and CFD by modified finite volume method. *Am Soc Mech Eng Press Vessels Pip Div (Publ) PVP.* 1998;377:79-83.

41. Aksenov A, Dyadkin A, Luniewski T, Pokhilko V. Fluid structure interaction analysis using Abaqus and FlowVision. Paper presented at: Proc. Abaqus User Conference 2004.

42. Cook RD. *Concepts and Applications of Finite Element Analysis.* John wiley & sons; 2007.

43. Zienkiewicz O, Taylor R, Zhu JZ. *The Finite Element Method: its Basis and Fundamentals.* Butterworth-Heinemann; 2005.

44. Ogden RW. Large deformation isotropic elasticity–on the correlation of theory and experiment for incompressible rubberlike solids. *Proc R Soc Lond A Math Phys Sci.* 1972;326(1567):565-584.

45. Martin C, Sun W. Biomechanical characterization of aortic valve tissue in humans and common animal models. *J Biomed Mater Res A.* 2012;100(6):1591-1599.

46. Bailey J, Curzen N, Bressloff NW. Assessing the impact of including leaflets in the simulation of TAVI deployment into a patient-specific aortic root. *Comput Methods Biomech Biomed Engin.* 2016;19(7):733-744.

47. Dellimore K, Kemp I, Scheffer C, Weich H, Doubell A. The influence of leaflet skin friction and stiffness on the performance of bio-prosthetic aortic valves. *Australas Phys Eng Sci Med.* 2013;36(4):473-486.

48. Bridio S, Luraghi G, Migliavacca F, Pant S, Garcia-Gonzalez A, Rodriguez Matas JF. A low dimensional surrogate model for a fast estimation of strain in the thrombus during a thrombectomy procedure. *J Mech Behav Biomed Mater.* 2023;137:105577.

49. Jiang H, Li J, Kong Y, et al. Fish swim bladders as valve leaflets enhance the durability of transcatheter aortic valve replacement devices. *Acta Biomater.* 2024;21:4.

50. Westerhof N, Lankhaar JW, Westerhof BE. The arterial Windkessel. *Med Biol Eng Comput.* 2009;47(2):131-141.

51. Pirola S, Cheng Z, Jarral OA, et al. On the choice of outlet boundary conditions for patient-specific analysis of aortic flow using computational fluid dynamics. *J Biomech.* 2017;60:15-21.

52. Xiao N, Alastruey J, Alberto FC. A systematic comparison between 1-D and 3-D hemodynamics in compliant arterial models. *Int J Numer Method Biomed Eng*. 2014;30(2):204-231.

53. Reymond P, Merenda F, Perren F, Rufenacht D, Stergiopulos N. Validation of a one-dimensional model of the systemic arterial tree. *Am J Physiol Heart Circ Physiol*. 2009;297(1):H208-H222.

54. Garcia D, Kadem L. What do you mean by aortic valve area: geometric orifice area, effective orifice area, or gorlin area? *Journal of Heart Valve Disease*. 2006;15(5):601-608.

55. Salmasi MY, Pirola S, Mahuttanatan S, et al. Geometry and flow in ascending aortic aneurysms are influenced by left ventricular outflow tract orientation: detecting increased wall shear stress on the outer curve of proximal aortic aneurysms. *J Thorac Cardiovasc Surg*. 2021; 166(1):11-21.

56. Hanna L, Armour C, Xu XY, Gibbs R. The Haemodynamic and pathophysiological mechanisms of calcific aortic valve disease. *Biomedicine*. 2022;10(6):1317.

57. Hellmeier F, Bruning J, Sundermann S, et al. Hemodynamic modeling of biological aortic valve replacement using preoperative data only. *Front Cardiovasc Med*. 2020;7:593709.

58. Gilmanov A, Barker A, Stolarski H, Sotiropoulos F. Image-guided fluid-structure interaction simulation of transvalvular hemodynamics: quantifying the effects of varying aortic valve leaflet thickness. *Fluids*. 2019;4(3):119.

59. Pirola S, Guo B, Menichini C, et al. 4D flow MRI-based computational analysis of blood flow in patient-specific aortic dissection. *IEEE Transac Biomed Eng*. 2019;1-1:3411-3419.

60. Armour CH, Guo B, Saitta S, et al. Evaluation and verification of patient-specific modelling of type B aortic dissection. *Comput Biol Med*. 2021;140:105053.

61. Manchester EL, Pirola S, Salmasi MY, O'Regan DP, Athanasiou T, Xu XY. Analysis of turbulence effects in a patient-specific aorta with aortic valve stenosis. *Cardiovasc Eng Technol*. 2021;12:438-453.

62. Cai L, Hao Y, Ma P, Zhu G, Luo X, Gao H. Fluid-structure interaction simulation of calcified aortic valve stenosis. *Math Biosci Eng*. 2022;19(12):13172-13192.

63. Chen Y, Luo H. A computational study of the three-dimensional fluid–structure interaction of aortic valve. *J Fluids Struct*. 2018;80:332-349.

64. Kadel S. *Computational Assessment of Aortic Valve Function and Mechanics under Hypertension*. Wright State University; 2020.

65. Nowak M, Divo E, Adamczyk WP. Fluid–structure interaction methods for the progressive anatomical and artificial aortic valve stenosis. *Int J Mech Sci*. 2022;227:107410.

66. Pil N, Kuchumov AG, Kadyraliev B, Arutunyan V. Influence of aortic valve leaflet material model on hemodynamic features in healthy and pathological states. *Mathematics*. 2023;11(2):428.

67. Amindari A, Kırkköprü K, İl S, Sünbüloğlu E. Effect of non-linear leaflet material properties on aortic valve dynamics - a coupled fluid-structure approach. *Eng Solid Mech*. 2021;9(2):123-136.

68. Hsu MC, Kamensky D, Bazilevs Y, Sacks MS, Hughes TJ. Fluid-structure interaction analysis of bioprosthetic heart valves: significance of arterial wall deformation. *Comput Mech*. 2014;54(4):1055-1071.

69. Thubrikar M. *The Aortic Valve*. CRC Press; 1990.

70. Li C, Tang D, Yao J, et al. Porcine and bovine aortic valve comparison for surgical optimization: a fluid-structure interaction modeling study. *Int J Cardiol*. 2021;334:88-95.

71. Cao K, Sucosky P. Aortic valve leaflet wall shear stress characterization revisited: impact of coronary flow. *Comput Methods Biomech Biomed Engin*. 2017;20(5):468-470.

72. Holzapfel GA, Gasser TC, Ogden RW. A new constitutive framework for arterial wall mechanics and a comparative study of material models. *J Elast Phys Sci Solids*. 2000;61(1–3):1-48.

73. Gasser TC, Ogden RW, Holzapfel GA. Hyperelastic modelling of arterial layers with distributed collagen fibre orientations. *J R Soc Interface*. 2006;3(6):15-35.

74. Morganti S. *Finite Element Analysis of Aortic Valve Surgery*. Universita degli Studi di Pavia, Italy; 2011.

75. Sun W, Li K, Sirois E. Simulated elliptical bioprosthetic valve deformation: implications for asymmetric transcatheter valve deployment. *J Biomech*. 2010;43(16):3085-3090.

76. Mao W, Li K, Sun W. Fluid-structure interaction study of transcatheter aortic valve dynamics using smoothed particle hydrodynamics. *Cardiovasc Eng Technol*. 2016;7(4):374-388.

77. Lior D, Puelz C, Edwards C, et al. Semi-automated construction of patient-specific aortic valves from computed tomography images. *Ann Biomed Eng*. 2022;51:189-199.

78. Ghosh RP, Marom G, Bianchi M, D'Souza K, Zietak W, Bluestein D. Numerical evaluation of transcatheter aortic valve performance during heart beating and its post-deployment fluid-structure interaction analysis. *Biomech Model Mechanobiol*. 2020;19:1725-1740.

79. Ezzat KA, Mahdy LN, Darwish A. Analysis of aortic valve using a finite element model. *Medical Informatics and Bioimaging Using Artificial Intelligence*. Springer Nature; 2022:195-206.